



FARM: A fully automated rice mapping framework combining Sentinel-1 SAR and Sentinel-2 multi-temporal imagery

Yuan Gao^{a,b,e}, Yaozhong Pan^{a,b,c,*}, Xiufang Zhu^{a,b}, Le Li^d, Shoujia Ren^{a,b}, Chuanwu Zhao^{a,b}, Xuechang Zheng^{a,b}

^a State Key Laboratory of Remote Sensing Science, Faculty of Geographical Science, Beijing Normal University, Beijing 100875, China

^b Key Laboratory of Environmental Change and Natural Disaster, Ministry of Education, Beijing Normal University, Beijing 100875, China

^c Academy of Plateau Science and Sustainability, Qinghai Normal University, Xining 810016, China

^d School of Management, Guangdong University of Technology, Guangzhou 510006, China

^e Beijing Engineering Research Center for Global Land Remote Sensing Products, Faculty of Geographical Science, Beijing Normal University, Beijing 100875, China

ARTICLE INFO

Keywords:

Rice identification

Training sample generation

Image segmentation

Sentinel

Phenology

Time-series satellite imagery

ABSTRACT

Rice farming exemplifies intensive agriculture, demanding significant inputs to achieve optimal yields. Thus, accurate and precise mapping of rice cultivation is vital for effective agricultural management and food security. However, such studies have been limited by the challenges of obtaining optical cloud-free data and dealing with radar data's speckle noise. Identifying crops using a single data source poses many difficulties. Additionally, acquiring sufficient representative training samples that accurately reflect diverse phenological patterns is challenging for large-scale monitoring and rice cultivation classification. To address these challenges, this study proposed a fully automated rice-mapping framework (FARM) that combines the strengths of time-series synthetic aperture radar (SAR) and optical satellite imagery for large-scale rice mapping without manual sample collection. First, an object-based, fully automatic training sample generation strategy is introduced. The phenology constraint rule, based on time-series SAR satellite images and specific rice-flooding features, is used to extract rice sample objects. Second, the extracted rice sample objects, adhering to phenological rules, serve as training samples for paddy rice extraction by integrating multiple random forest (RF) classifiers, referred to as the multi-RF method, where each RF is individually built using images acquired during each phenological phase of the growing season. Furthermore, the study explored the availability of the method in early-season rice identification by transferring the training samples acquired by the FARM to a new year. The proposed FARM approach was then validated under different cropping conditions at three study sites in China and two sites in other countries. The results showed that the FARM framework proved to be more effective than other methods at all five study sites, achieving average overall accuracies (OA) ranging from 89.67%–97.00%. In addition, when transferring the training samples from 2021 to other years (2020/2022), the OAs of site A, site B and site C were high during the heading period, with accuracies of 97.57%, 84.28% and 89.27%, respectively. These results demonstrated that, first, the FARM framework exhibits high efficiency and accuracy in different study areas without the need for extensive fieldwork to collect training samples. Second, the method has good performance in the early-season rice mapping of the new year and can be used to perform timely and accurate rice identification and monitoring tasks. The method shows great potential in obtaining large-area automatic rice mapping results in a timely and accurate manner. The latest release of FARM can be viewed at <https://feature-selected.users.earthengine.app/view/farm>, and the code is available on GitHub at the link <https://github.com/gactyxc/FARM.git>.

1. Introduction

Paddy rice is a fundamental food source for a significant proportion of the global population, primarily in underdeveloped areas of Asia,

Latin America and Africa. Therefore, accurately monitoring rice areas is indispensable to guaranteeing worldwide food safety. In addition, with its special flooding characteristics, rice cultivation has a considerable impact on water usage and the release of greenhouse gases (Dong and

* Corresponding author.

E-mail address: pyz@bnu.edu.cn (Y. Pan).

<https://doi.org/10.1016/j.compag.2023.108262>

Received 6 May 2023; Received in revised form 10 September 2023; Accepted 15 September 2023

0168-1699/© 2023 Elsevier B.V. All rights reserved.

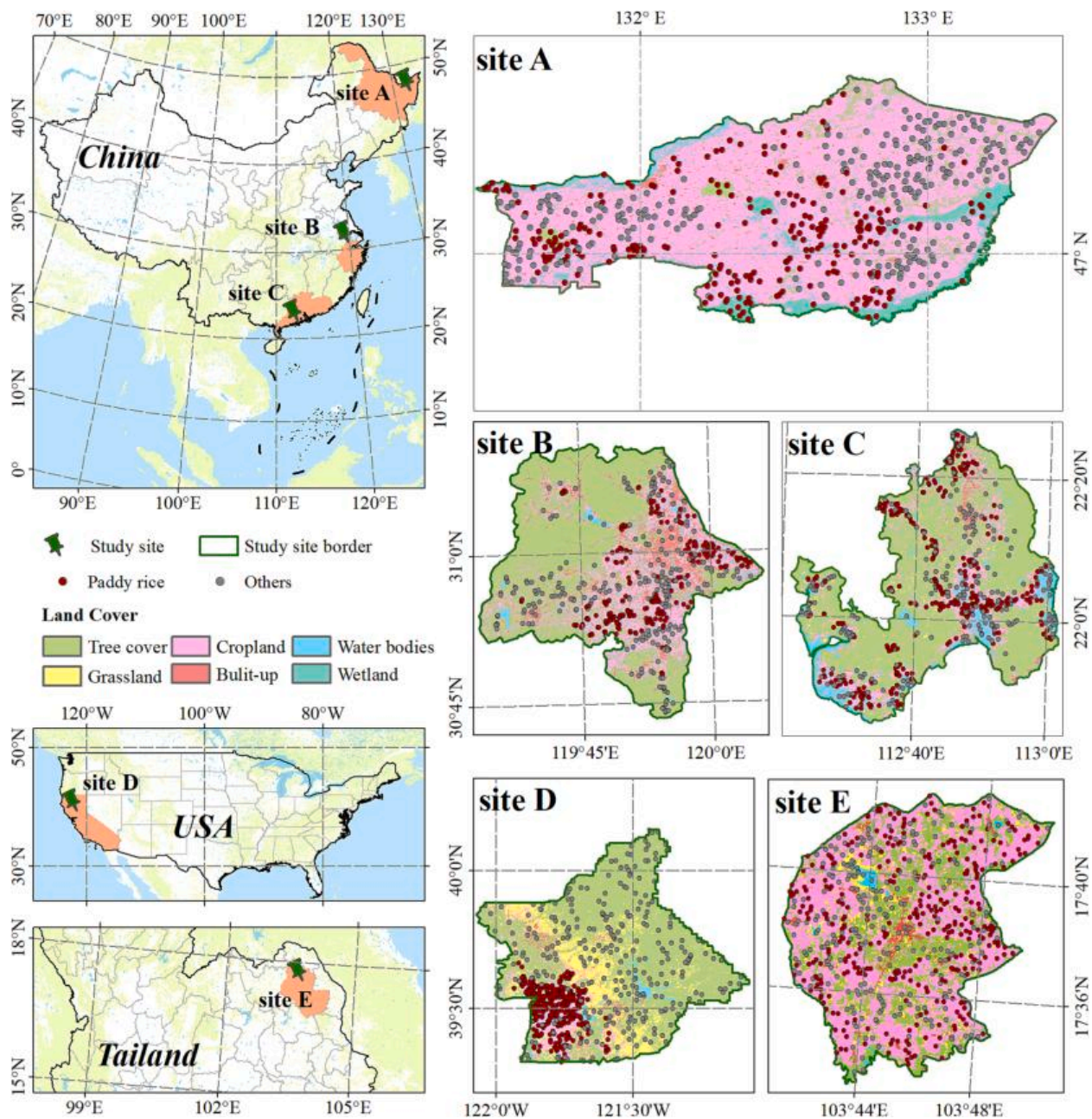


Fig. 1. Study area and sample points in 2021. The land cover map is from ESA WorldCover 10 m 2021 (<https://esa-worldcover.org/en>).

Xiao, 2016; Keppler et al., 2006; Linquist et al., 2012), so accurately describing rice-growing areas is also important for studies of climate change and for water resource monitoring. Given the advancements in remote sensing techniques and the availability of open-source satellite image data sources like Moderate resolution Imaging Spectroradiometer (MODIS), Landsat and Sentinel, it has become feasible to use remote sensing to obtain the spatial distributions of crops at large scales and to realize the real-time monitoring of crops (Dong et al., 2016; Dong and Xiao, 2016; Ni et al., 2021; Weiss et al., 2020; Zhan et al., 2021; Zhang et al., 2022).

Optical-derived mapping methods for rice cultivation typically rely on the spectral bands or vegetation indices that exhibit sensitivity towards a combination of water bodies, soil, and vegetation, as paddy rice is the only staple crop that requires transplanting (Dong and Xiao, 2016). Several studies have been conducted based on the unique temporal variations in the water-soil-vegetation composition that can be applied to paddy rice identification (Chen et al., 2011; Jin et al., 2016;

Qin et al., 2015; Son et al., 2021, 2014; Xiao et al., 2002). For example, Xiao et al. (2002) derived the distribution of rice by utilizing the correlation between the normalized difference vegetation index (NDVI) / enhanced vegetation index (EVI) and land surface water index (LSWI) to extract flooding and transplanting signals. However, collections of optical images of the whole phenological stage can provide sufficient information for rice identification. Unfortunately, most rice grows in cloudy and rainy areas, and it is difficult to obtain clear images during crucial phenological stages of rice growth.

Another approach to mapping paddy rice is through the use of machine learning, which is less dependent on images taken during a particular transplanting period. By establishing mathematical connections between the input data obtained from the phenological traits of rice during the non-transplanting period and the training samples, these methods can effectively map rice fields (Wang et al., 2019; Weiss et al., 2020; Zhang et al., 2022). Nevertheless, because generating training sample sets can be labor-intensive and spatiotemporal spectral

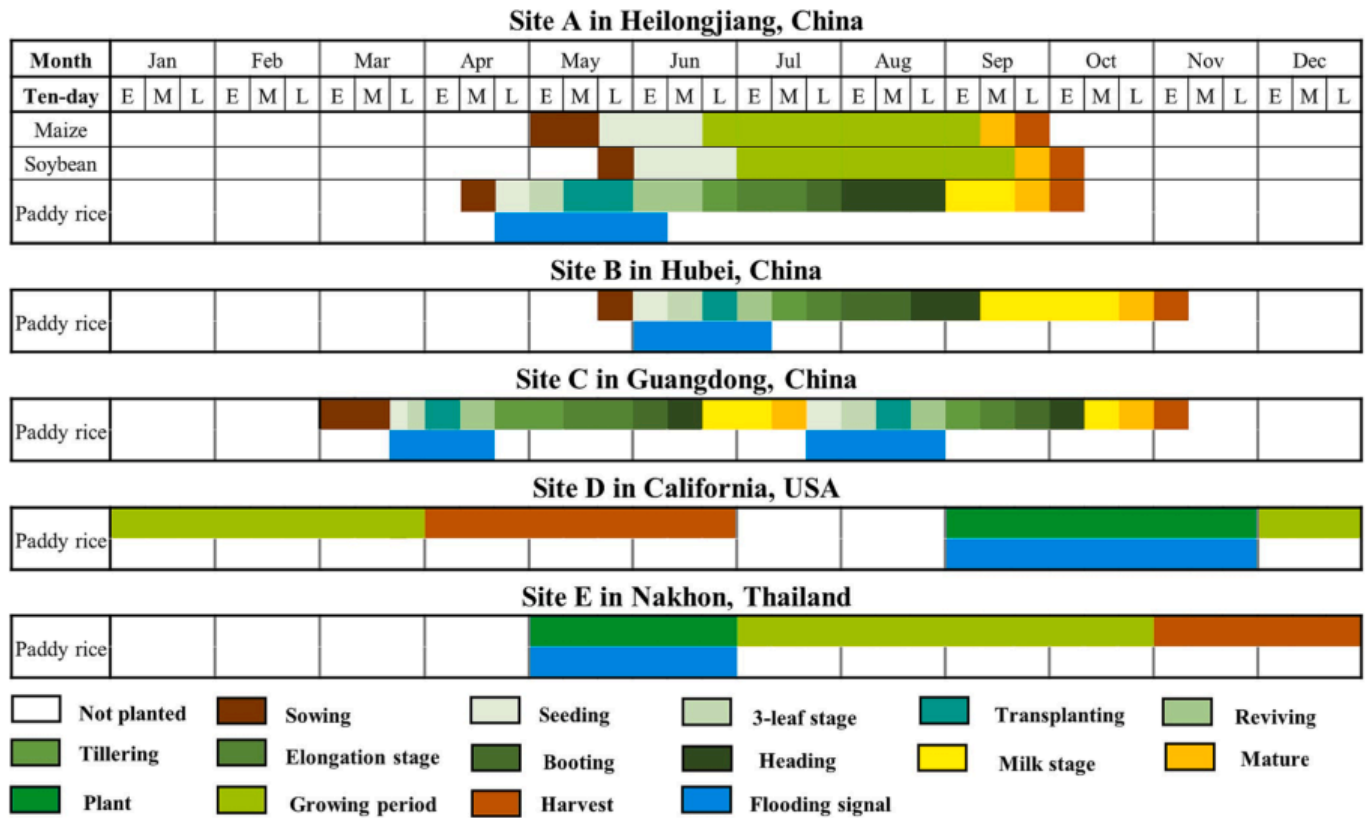


Fig. 2. Phenological conditions of different crops at each study site.

variabilities can affect results, automated rice mapping on a large scale is challenging (Xiong et al., 2017; Xuan et al., 2023). Therefore, the automatic generation of high-quality training data, which can be reused, has the potential to automate the mapping of rice and significantly reduce associated costs.

Many researchers have addressed this issue and developed various methods for automatic sample generation. For instance, Hao et al. (2020) proposed a transfer learning workflow that utilizes a classification model trained with high-confidence pixels from the Cropland Data Layer (CDL) in the contiguous United States of America (CONUS) to identify crop types in other regions. However, the global rice planting structure is complex, and relying solely on the CDL may not capture the diverse planting patterns of rice cultivation. In response to this challenge, other researchers have proposed a flexible framework that combines phenological target crop mapping with machine learning. They utilize cloud-free time series satellite images in specific regions to generate target crop potentials and train a classifier for automatic crop mapping in large cloudy areas (Zhang et al., 2021, 2022). Nonetheless, this approach requires having cloud-free images available during critical phenological periods, which limits its applicability in areas with frequent cloud cover or heavy rainfall.

As opposed to optical imagery, synthetic aperture radar (SAR) data has gained popularity in cloudy regions due to its unique ability to penetrate through clouds and provide accurate readings on characteristics of ground targets pertaining to electromagnetics and structure (Bouvet and Le Toan, 2011; Zhan et al., 2021). A prevalent approach to map rice using SAR data is to construct a tree model with threshold-based decision making. The primary factors commonly utilized for the decision tree are the changes in radar backscatter values throughout the rice growth stage, characterized by either dynamic range or variance (Nguyen et al., 2016; Xu et al., 2023; Zhan et al., 2021). Characteristics throughout the entire growth period of rice may diminish its unique flooding properties, making it challenging to differentiate rice from

other crops with comparable backscatter dynamic ranges. As a result, Zhan et al. (2021) leveraged the distinctive “V”-shaped pattern in the time series of Sentinel-1A VH backscatter, which emerges as a result of flooding pre- and post-rice transplanting, to accurately map rice fields. Despite the advances in SAR technology, the accuracy of classifying paddy fields from SAR images is still limited by speckles. To overcome this challenge, researchers are turning to the object-based classification approach as a promising method to improve the identification of paddy fields (Luo et al., 2021; Xu et al., 2023; Yang et al., 2021). Nevertheless, for regions with complex planting structures and fragmented land parcels, depending solely on SAR data may not yield satisfactory results. Therefore, integrating the strengths of both SAR and optical imaging modalities can lead to a more reliable and accurate identification of paddy fields.

The main emphasis of this study is on developing a fully automated rice-mapping framework (FARM) that integrates the benefits of time-series SAR and optical satellite imagery for large-scale applications, leveraging the unique temporal variations of rice in the water-soil-vegetation composition. The objectives of this study are: (1) to develop a fully automatic training sample generation strategy based on special rice-flooding features using long-term Sentinel-1 SAR satellite images; (2) to design a robust multiple random forest (RF) classifier fusion mapping framework to complete rice mapping by utilizing all available optical and SAR satellite images at different study sites; and (3) to further evaluate the transferability of the FARM framework by applying the training samples to different years and regions.

2. Study sites and data

2.1. Study sites

The growth and development of a crop can vary depending on factors such as the specific crop varieties used, the prevailing environmental

conditions, and the decisions made by farmers. As a result, the phenological stages and growth conditions of the same crop can differ between various regions (Pan et al., 2012). To address the complex characteristics of rice-growing areas, we selected a total of five study sites to evaluate the effectiveness of our proposed framework (Fig. 1), including three sites in China, one site in the United States of America (USA), and one site in Thailand.

In China, rice is widely cultivated with various planting patterns. For this study, we carefully selected three different planting patterns representing regions with varying scales of rice cultivation, ranging from south to north, as our study sites (site A-C). Site A is Fujin city, Heilongjiang Province (130°13'–135°05'E and 45°01'–48°27'N), covering an area of 8,227.16 km², located in northern China, with a moderate temperate monsoon continental climate. All crops at site A are one-season crops. In addition to rice, the major crops include corn and soybeans. Typically, rice cultivation involves sowing in early April followed by transplantation in mid-May. The growth period of rice spans around 4–5 months, and the crop is commonly harvested towards the end of September (Fig. 2). Site B is Changxing city, Hubei Province (112°13'–112°31'E and 30°12'–30°25'N), covering an area of 1,430 km², located in the central part of China, with a subtropical humid monsoon climate. Due to the abundant rainfall in this area, various types of crops, such as various oil crops, cotton, and rice, are planted. As shown in Fig. 2, rice is usually sown in late May and transplanted around late June. Site C is Taishan city, Guangdong Province (111°59'–113°15'E and 21°27'–22°31'N), covering an area of 3,308.24 km², located in the southwestern region of the Pearl River Delta with a humid tropical and subtropical monsoon climate. In site C, the terrain varies significantly, with the southern section being relatively flat and the central and northern parts featuring mountains. Rice cultivation in this region is sporadic. Typically, double-cropping is practiced, and farmers grow a mix of crops, including double rice, peanuts, tubers, and vegetables. Among them, early rice is sown in late March, transplanted in early April, and harvested by mid-July. Late rice is then transplanted immediately following the harvest of early rice, as depicted in Fig. 2. In this study, only late rice was analyzed and mapped at site C to facilitate comparisons with the other study areas and other methods.

Except for the three sites in China, two additional sites in other countries were selected to test the robustness of the proposed method. Site D is located in Butte, California, USA (121°4'–122°4' W and 39°18'–40°9'N), covering an area of 4,340 km². It is situated in the northern part of California, specifically in the Sacramento Valley region, where rice is the main cultivated crop. Typically, rice planting occurs in September, and the crop is transplanted before November. The harvest of the rice crop takes place in April of the following year, aligning with the local growing season, as shown in Fig. 2. Site E is located in Sakon, Nakhon, Thailand (103°41'–103°51'E and 17°33'–17°43'N), covering an area of 651 km². This site is situated in the northeastern part of Thailand. The favorable climate and fertile soil make it suitable for growing rice, and the rice is usually sown in May and transplanted around late June (Fig. 2).

2.2. Satellite imagery

The study utilized satellite imagery provided by the European Space Agency (ESA), which included Sentinel-1 and Sentinel-2 satellite images. Sentinel-1, equipped with a single C-band SAR instrument operating at 5.405 GHz, is recognized as one of the most extensively utilized radar satellites. For this study, all available Level 1 GRDH (ground-range detected high resolution) images acquired over each study site in 2021 and 2022 from Google Earth Engine (GEE) (<https://earthengine.google.com/>) were used for training sample generation and classification. The GRDH product has a spatial resolution of 5 m × 20 m and is acquired in interferometric wide swath (IW) mode with dual polarization (VH and VV).

Sentinel-2, an optical satellite comprising two complementary

Table 1

Download links for related datasets applied in this study.

Datasets	Data source
Crop calendar of China	https://zdcscx.moa.gov.cn:8080/nyb/pc/calendar.jsp
Crop calendar of Thailand	https://ipad.fas.usda.gov/rssiws/al/crop_calendar/seasia.aspx
Crop calendar of the US	https://ipad.fas.usda.gov/rssiws/al/crop_calendar/us.aspx
ESA WorldCover 10 m 2021	https://esa-worldcover.org/en
CDL data	https://www.nass.usda.gov/Research_and_Science/Cropland/Release/
Global Agricultural Monitoring	https://glam1.gsfc.nasa.gov/

satellites (Sentinel-2A and Sentinel-2B), operates with a 5-day revisit cycle for image acquisition. The spatial resolution varies across different bands, with 10 m for Bands 2, 3, 4, and 8, 20 m for Bands 5, 6, 7, 8A, 11, and 12, and 60 m for Bands 1, 9, and 10. Starting from January 25, 2022, the DN (digital number) values for Sentinel-2 scenes with PROCESSING_BASELINE '04.00' or higher have been shifted by 1000 to harmonize the data. The HARMONIZED collection adjusts the data in newer scenes to match the same range as in older scenes ("Sentinel-2 Datasets in Earth Engine | Earth Engine Data Catalog," n.d.). For this study, we selected all valid Sentinel-2 Level-2A imagery from the 'S2_SR_HARMONIZED' data collection in GEE over site A-E in 2021, site A in 2020, and site B-C in 2022 for rice mapping.

2.3. Ancillary data

In order to conduct crop phenology analyses at the study sites, ancillary data, including crop calendar data for 2020–2022 and land cover samples, were utilized. The crop calendar data in each study site were sourced from the Ministry of Agriculture of the People's Republic of China and the Foreign Agricultural Service of United States Department of Agriculture (Table 1).

For the three study sites in China, the land cover samples were identified by utilizing ground survey data and high-resolution images from Google Earth. A total of 534, 496, and 466 samples were selected for site A, site B and site C, respectively, as illustrated in Fig. 1 and Table 2. It is important to note that these samples were split into training (30%) and validation (70%) sets for crop characteristic analysis and classification accuracy assessment. For site D, the land cover samples were initially randomly selected using the CDL, and later cross-referenced and refined with high-resolution images obtained from Google Earth. In the case of site E, land cover samples were also randomly selected and then corrected using high-resolution images. Eventually, a total of 600 samples were carefully chosen for site D, while an equal number of 600 samples were selected for site E.

3. Fully Automated Rice Mapping (FARM) framework

A fully automated rice mapping framework (FARM) was proposed in this study (Fig. 3), which mainly consists of five steps: (1) data pre-processing of Sentinel-1 and Sentinel-2 images; (2) generating paddy rice training samples; (3) extracting paddy rice using multiple random forest (RF) classifiers, referred to as the multi-RF method, where different RFs are built based on images acquired in different growth phases of the growing season; (4) updating the training samples and rice maps for adjacent years using the spectral angle distance (SAD); and (5) applying the method to map the rice-cultivated area, evaluating its performance, and comparing it with the performance of rule-based classifiers. All of the aforementioned procedures were carried out using Google Earth Engine (GEE).

Table 2
The sample number for each land cover type at the five study sites.

	Rice	Maize	Soybean	Other crops	Woodland	Wetland	Water	Built-up
Site A	283	70	117	0	5	30	17	12
Site B	241	0	0	124	38	0	45	48
Site C	275	0	0	71	36	0	42	42
Site D	293	0	0	68	206	4	12	17
Site E	345	0	0	96	120	0	18	21

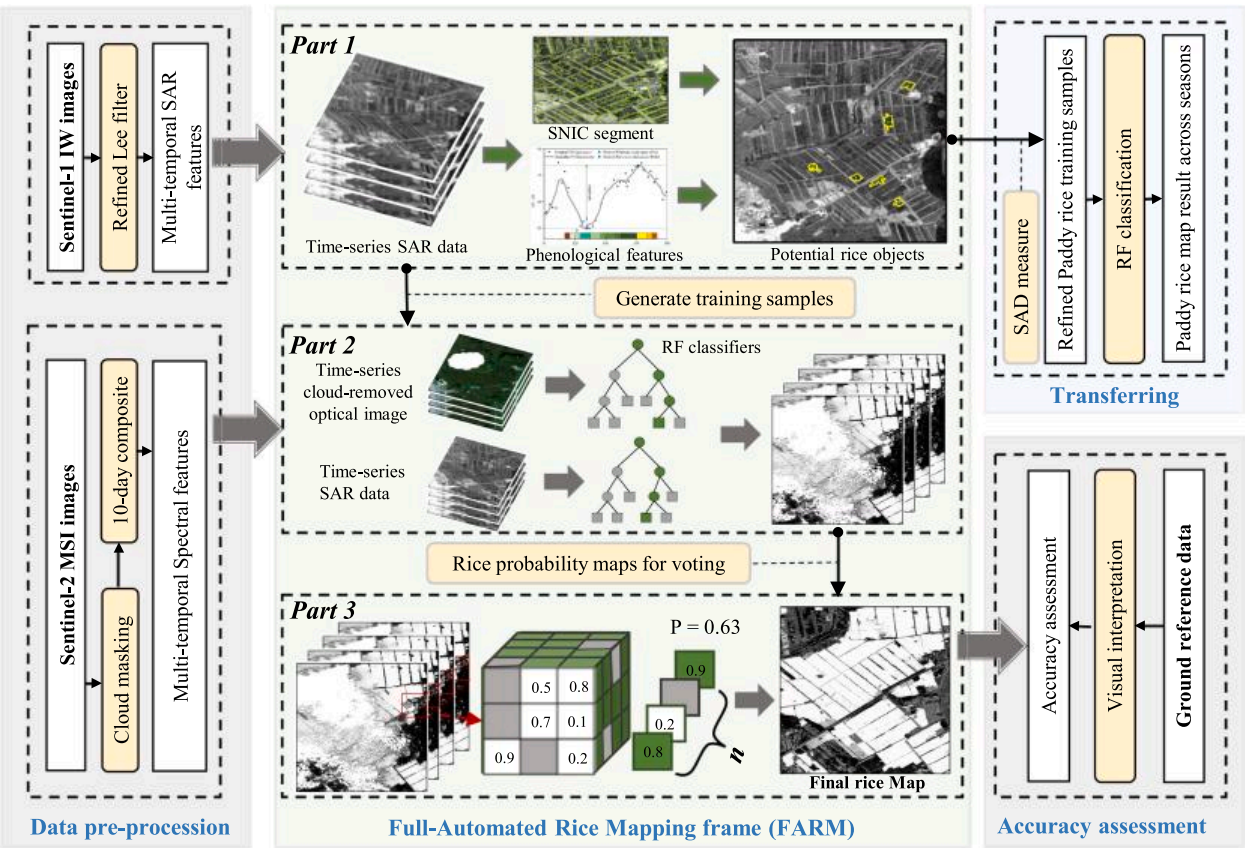


Fig. 3. The methodological workflow of the FARM framework for rice mapping implemented in this study.

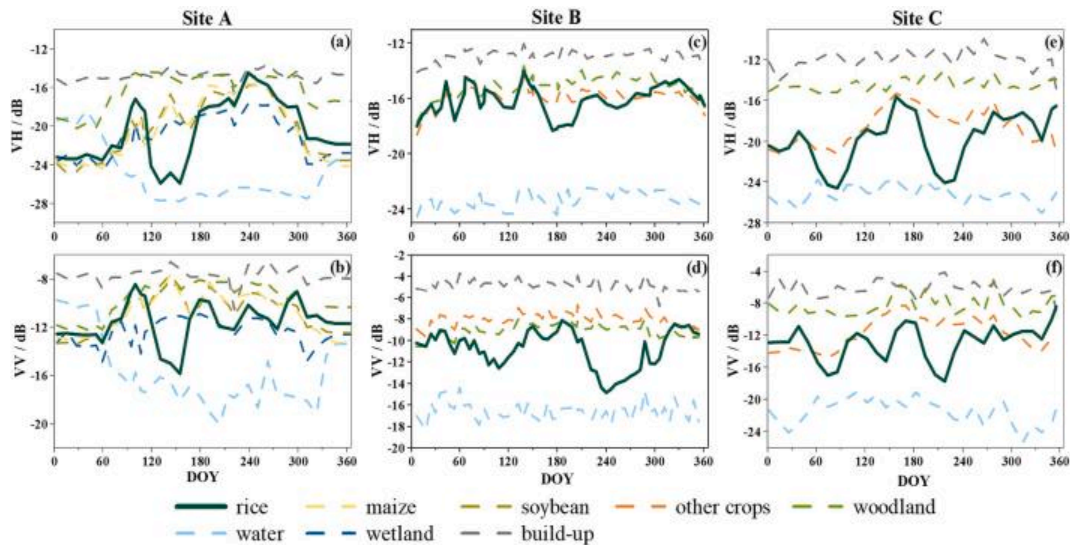


Fig. 4. Temporal profiles of the VH and VV of rice and non-rice samples at study sites A-C.

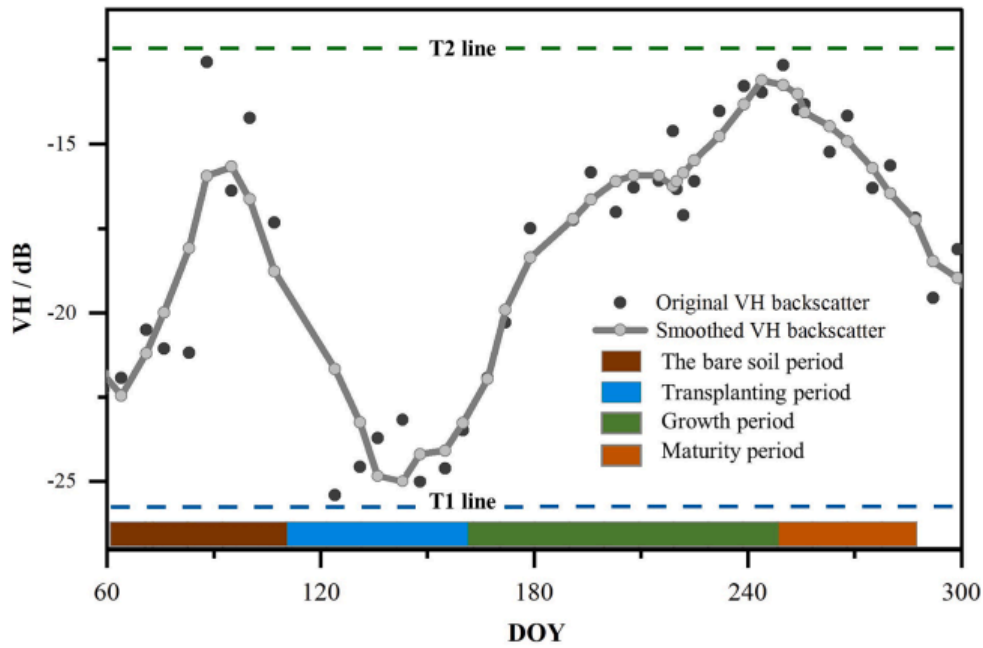


Fig. 5. Diagram of VH time series curves for designing the paddy rice extraction rule.

3.1. Data preprocessing

3.1.1. Sentinel-1 data

The following steps were taken in the preprocessing of the Sentinel-1 images: (1) applying an orbit file using reprojected orbits and removing thermal noise at the scene edges in the range direction; (2) performing radiometric calibration to convert pixel values into SAR backscatters represented in sigma naught (s^0); (3) conducting terrain correction using a 1-arcsecond resolution Shuttle Radar Topography Mission (SRTM) digital elevation model (DEM) to eliminate terrain effects and resampling the output to a resolution of $10\text{ m} \times 10\text{ m}$; (4) applying a refined Lee filter with a window size of 7×7 to reduce speckle noise; and (5) transforming sigma naught (s^0) values into dB units using Eq. (1):

$$DN_{dB} = 10 \times \log_{10}s^0$$

where DN_{dB} refers to the backscatter output in dB units.

3.1.2. Sentinel-2 data

In order to obtain high-quality Sentinel-2 imagery for rice mapping, we utilized the Sentinel-2 quality assessment (QA60) band to mask out any contaminated pixels caused by opaque and cirrus clouds. Subsequently, we produced a 10-day median composite image during the rice growing seasons, as this compositing approach has proven successful in numerous studies across a range of classification tasks (Yang et al., 2021).

3.2. Automatic generation of training samples for paddy rice

3.2.1. Spatial objects extraction using SNIC

Identifying homogeneous regions from multiple land cover classifications in Sentinel-1 imagery is crucial for the automatic generation of training data. For image segmentation, the study employed Simple non-iterative clustering (SNIC), which involved dividing the original image into multiple super-pixels. Subsequently, a clustering algorithm was used to group together homogeneous pixels by optimizing the minimum distance between candidate pixels and the cluster centroid in an iterative manner, based on selected features (Achanta and Süsstrunk, 2017).

The use of multi-temporal metrics has been well-established in land-cover segmentation and classification (Hansen et al., 2014), as they can

identify temporal patterns even in irregularly spaced time series. In this study, the temporal evolution of the σ_0 time series for nine different land-cover classes at the study site A was analyzed to examine the evolution processes (Fig. 4). As shown in Fig. 4, the σ_0 value of rice is higher at the growth peak and lower during the transplanting period. Additionally, compared to other crops, the transplanting signal of rice causes it to have higher σ_0 time-series amplitudes, and this is manifested by a larger standard deviation in the temporal polarization values. Specifically, to make full use of different polarization images and reduce the impact of extreme noise, the 50th-percentile VH polarization for 2021 (referred to as Median (VH_{year})), the standard-deviation VH polarization for 2021 (referred to as STD (VH_{year})), and the 5th-percentile VV polarized data for 2021 (referred to as Min (VV_{year})) were calculated and chosen as the input features for the final SNIC segmentation method. For each pixel in the study area, three temporal metrics were calculated: Median (VH_{year}), STD (VH_{year}) and Min (VV_{year}). These metrics were then used to generate three band images, which were utilized as inputs for the segmentation process. The resulting segmented images were exported from the GEE platform, retaining the original coordinate reference system, and with a pixel resolution of 10 m.

The SNIC algorithm comprises three main steps. Firstly, it initializes the centroid pixels on a regular grid within the image. Then, it computes the Euclidean distance between each pixel in the five-dimensional space of spatial coordinates and input features to determine its dependence on the centroid. Finally, by integrating the normalized spatial and color distances, the distance function generates efficient, compact, and almost uniform polygons. The SNIC algorithm has several key parameters, including “image,” which represents the feature image used for segmentation, “size,” which specifies the spacing of super-pixel seed positions based on pixels, “compactness,” which affects the shape of the clusters, “connectivity,” which specifies the type of contiguity used to merge adjacent clusters, and “neighborhood size,” which avoids tile boundary artifacts. For this study, feature images with previously calculated Median (VH_{year}), STD (VH_{year}) and Min (VV_{year}) values were used. The value of the “compactness” parameter affected the shape of the resulting parcels, with larger values producing square-shaped segments, while smaller values led to more rectangular segments. In this study, the “size,” “compactness,” “connectivity,” and “neighborhood size” parameters were set to 36, 5, 8, and 256, respectively, as described in Yang et al. (2021).

3.2.2. Recognition of paddy rice objects

(1) Distinguishing paddy rice objects from non-crop objects

The σ_0 signal of rice fields exhibits distinct minima during the flooded phase and maxima during the heading stage of rice plants *ADDIN* (Clauss et al., 2018; Kuenzer and Knauer, 2013; Nguyen et al., 2015). Meanwhile, Fig. 4 demonstrates that water and aquaculture consistently have low backscatter values throughout the year, significantly lower than rice's minimum backscatter. Conversely, urban areas and natural vegetation consistently have high backscatter values, generally exceeding those observed during the entire rice growth season. Exploiting these distinctions, we establish straightforward rules to differentiate rice fields from non-crop objects. Specifically, water and aquaculture, with low backscatter year-round, are excluded using the VH backscatter mean. Urban areas and natural vegetation, characterized by high backscatter, are excluded using the VH backscatter minimum during the rice growth season (Eq. (2)).

$$\text{median}(VH_{\text{year}}) \geq T1 \text{ and } \min(VH_{\text{grow}}) \leq T2 \quad (2)$$

where $\text{median}(VH_{\text{year}})$ and $\min(VH_{\text{grow}})$ represent the median and maximum values, respectively, between the whole growing period of VH.

The determination of T1 and T2 values followed a simple statistical approach based on the backscattering intensity of natural vegetation and temporary water objects (Xu et al., 2023). Firstly, the rule ($NDVI_{\text{max}} > 0.3$) was applied to detect natural vegetation objects, while the rule ($NDVI_{\text{max}} > 0.4$ and $NDWI_{\text{max}} > 0.3$) was used for detecting temporary water objects. The T1 value was then calculated as the 50th percentile of the annual median backscattering intensity of all temporary water objects, whereas the T2 value was determined as the 25th percentile of the annual minimum backscattering intensity of all natural vegetation objects. Based on our study of site A-C in China and relevant work by (Zhan et al., 2021), we set the default value of T1 for the entire country as -20 . For central and southern China (i.e., study sites B and C), the default value of T2 was set as -17 , whereas for northern China (i.e., study site A), it was set as -20 .

(2) Distinguishing paddy rice objects from other crop objects.

Due to similar time profiles between crops (Fig. 4), paddy rice cannot be effectively distinguished from other crops using the extreme VH values alone. As Fig. 5 shows, the development of paddy rice can be divided into four distinct stages: (1) the bare soil period; (2) transplanting period; (3) growth period; and (4) maturity period (Dong and Xiao, 2016).

As the only crop that requires a significant amount of water during transplanting, paddy rice shows obvious characteristic signals of 'soil-water' and 'water-vegetation' before and after rice transplanting, appearing as a "V" shape (that is, first falling and then rising) on the backscattering time trajectory (Zhan et al., 2021). Therefore, a rule dictating the phenological constraint of the "V"-shaped feature in the time series of Sentinel-1 VH backscatter was established (Eq. (3)):

$$\text{slope}(\text{Rice}_{\text{sowing-transplanting}}) < 0 \text{ and } \text{slope}(\text{Rice}_{\text{transplanting-growing}}) > 0 \quad (3)$$

where $\text{slope}(\text{Rice}_{\text{sowing-transplanting}})$ refers to the slope of the VH backscatter time series during the sowing-transplanting period; and $\text{slope}(\text{Rice}_{\text{transplanting-growing}})$ refers to the slope of the VH backscatter time series during the transplanting-growing period.

Finally, to ensure the removal of possible random noise from the Sentinel-1 imagery, only spatial objects conforming to the predefined rules were retained and automatically labeled as paddy rice.

3.3. Multi-RF mapping framework for paddy rice

To minimize the impact of radar image speckle noise, an object-based method for automatic generation of training samples was used.

However, the fully object-oriented classification method overly relies on the accuracy of segmented objects and thus may lead to serious omissions (Belgiu and Csillik, 2018). Although the Sentinel-2 optical image data are easily affected by the weather conditions, making it impossible to obtain effective and complete time-series data in a large area, they contain more spectral information in cloud-free areas and are not affected by speckle noise. Therefore, a framework for seamless mapping of paddy rice was developed by integrating optical and SAR data. The framework involves using Auto-generated training samples described in section 3.2 and multiple random forest (RF) classifiers in a multiple classifier fusion approach, which is referred as multi-RF. In contrast to prior research utilized full time-series images to derive classification results, our framework trained a distinct RF classifier for each phenological phase image. Fig. 3 illustrates the three parts of the classification framework.

Part 1: Pixels meeting the constraint rules shown in Eqs. (2)–(3) were selected as rice samples, while those not meeting Eqs. (2) and (3) were defined as non-rice samples.

Part 2: We trained two RF classifiers for each temporal image after generating the training samples in Part 1. The input features for each optical-based RF classifier included three vegetation indices: the NDVI, EVI and LSWI (Chandrasekar et al., 2010), and the input features of each SAR-based RF classifier included only the VH and VV backscatter values. For a given pixel, the RF output is the probability that the pixel represents rice, not the 0 (non-rice) and 1 (rice) binary map. For each RF classifier, we set the *ntree* (number of trees) to 100 and used the default setting for *mtry* (subset of variables randomly selected at each node), which is the square root of the number of variables. Using these settings, we generated multi-temporal probability maps of paddy rice from time-series optical and radar images.

Part 3: We calculated the average likelihood of each pixel being recognized as rice (Eq. (4)), and pixels polluted by clouds were not involved in the calculation. The label of pixel *i* was set to the class with the higher likelihood.

$$P_i = \frac{\sum_{j=1}^m p_{ij}}{m} \quad (4)$$

where P_i refers to the likelihood that pixel *i* was classified as rice; *m* refers to the number of cloudless images; and p_{ij} refers to the likelihood that pixel *i* was classified as rice in image *j*.

3.4. Performance evaluation of FARM framework

3.4.1. Accuracy assessment of the rice maps

In this study, the classification accuracy of the proposed FARM framework was assessed by five validation metrics, including the overall accuracy (OA), user's accuracy (UA), producer's accuracy (PA), and the *F1-score*, which were all calculated from the confusion matrix. Specially, the *F1-score* were calculated as follows (Hripcsak and Rothschild, 2005):

$$F1\text{score} = 2 \times \frac{UA \times PA}{UA + PA} \quad (5)$$

3.4.2. Comparative analysis of the FARM with other methods for rice mapping

The performance of the FARM framework with other rice-mapping approaches was compared based on the metrics described in Section 3.4.3. First, the two most recent rule-based methods using only Sentinel-1 data from Zhan et al. (2021) and Xu et al. (2023) were selected for comparison (referred to as $VH_{\text{pixels}}\text{-SARFS}$ and $VH_{\text{objects}}\text{-SPRI}$, respectively). The key feature for rice identification in these two methods was the dynamic range and trends of SAR backscatter during the rice growing period. Specifically, all the thresholds in $VH_{\text{pixels}}\text{-SARFS}$ were set to 0. For $VH_{\text{objects}}\text{-SPRI}$, the 20th percentile was used for *v* determination at each study site, and the 20th, 80th, and 80th percentiles were used for *w* determination at study site A, study site B and study site C,

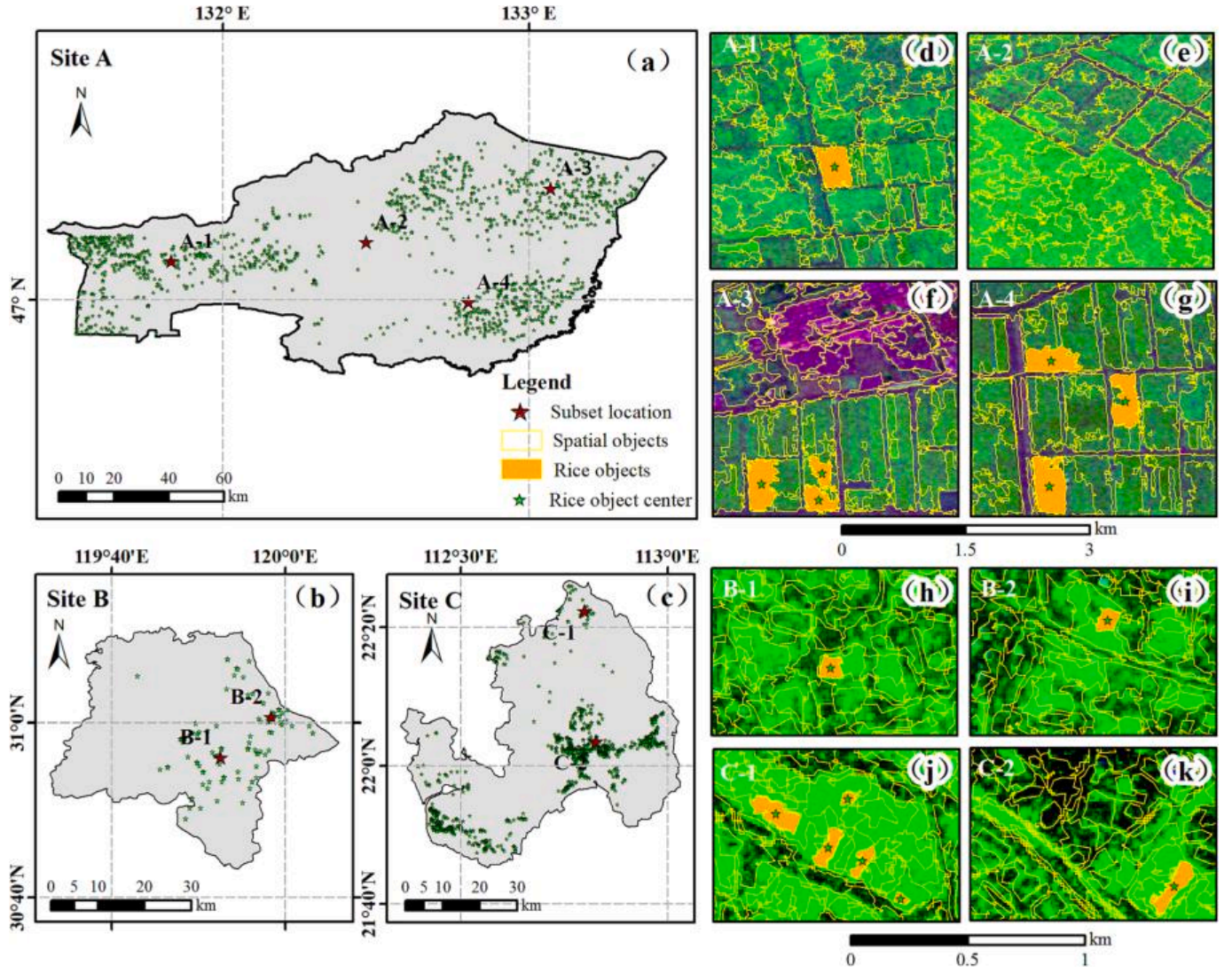


Fig. 6. The distribution of paddy rice training samples produced from the Sentinel-1 imagery of 2021 was examined for each study site (a-c), and eight subsets featuring paddy rice objects from three study sites were analyzed in detail (d-k). These samples are superimposed over the SAR features (R: Median (VH_{year}), G: STD (VH_{year}), and B: Min (VV_{year})).

respectively. Additionally, the RF classifier used only the key SAR features, including the maximum value, minimum value and median VV and VH backscatter values, covering the whole growth period (referred to as $SAR_{objects-RF}$) (Luo et al., 2021), and the RF classifier used only the key optical features, including the maximum, minimum and median NDVI, EVI and LSWI values, throughout the whole growth period (referred to as $Optical_{pixels-RF}$) (Belgiu and Csillik, 2018) for the comparison.

3.4.3. Transfer of training samples across years

The variability of land cover types may impact the ability to reuse reference data across different spatial and temporal contexts. To achieve both cost reduction in annual reference data collection and ensure the usability of samples in early-season rice identification across different years, we adopt a simple SAD (spectral angle distance)-based method to update the training data of paddy rice across seasons (Yang et al., 2021).

Initially, Eq. (6) (Pan et al., 2017) was employed to compute the SAD values of the Sentinel-2 images in both the reference and target years on a monthly basis. These values were then considered as the probability of alterations in land cover. The training data update method involves primarily removing samples that have experienced changes in land cover types. In the target year, after comparing the SAD values of land

cover types with and without changes, only those samples with SAD values of less than 0.1 in all months were selected as consistent training samples (Yang et al., 2021). Finally, the rice distribution map of the target year was efficiently and timely produced by the FARM framework with updated training samples. In order to assess the effectiveness of the sample updating strategy, site A was evaluated in 2020 while site B and site C were evaluated in 2022, as there were no SAR images available on a large scale for site A in that year. Specifically, this study updated the samples from 2021 to the heading growing stage of 2020/2022 based on the above strategy and used the updated sample to identify rice and evaluate the effectiveness of the sample update strategy and the effectiveness of the sample for early-season rice identification of rice in the new year:

$$SAD(\mathbf{A}, \mathbf{B}) = \arccos\left(\frac{\mathbf{AB}}{\|\mathbf{A}\| \|\mathbf{B}\|}\right) = \arccos\left(\frac{\sum_{i=1}^n \mathbf{A}_i \mathbf{B}_i}{\sqrt{\sum_{i=1}^n \mathbf{A}_i^2} \sqrt{\sum_{i=1}^n \mathbf{B}_i^2}}\right) \quad (6)$$

where \mathbf{A} is the spectral vector of the reference year, \mathbf{B} is the spectral vector of the target year, and n is the number of bands.

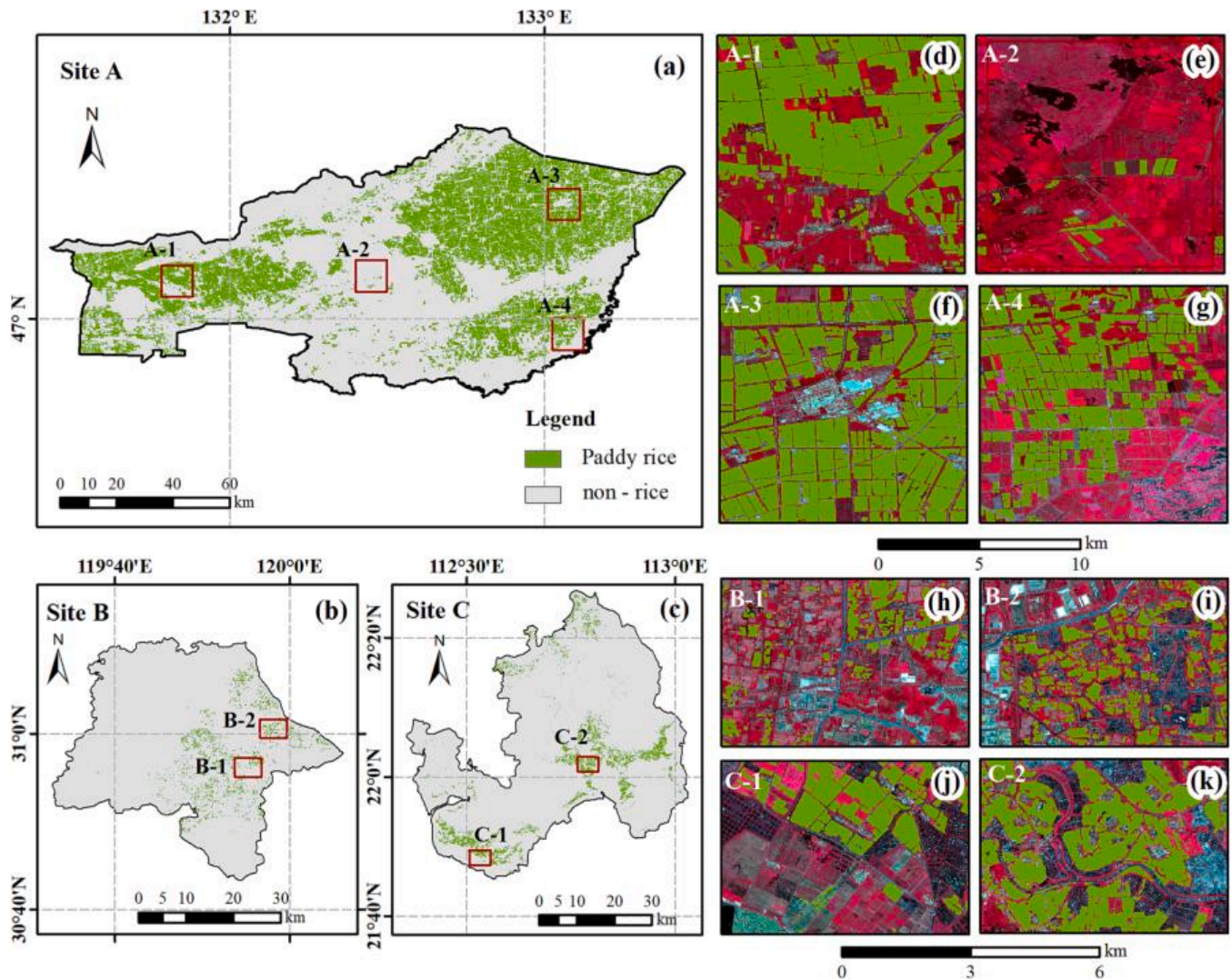


Fig. 7. Paddy rice distribution map produced by the proposed method at each study site (a-c) and close-up views of eight subsets with paddy rice objects at three study sites (d-k). The maps are superimposed over false-color composite Sentinel-2 images (R: NIR, G: Red, and B: Green). (For interpretation of the references to color in this figure legend, the reader is referred to the web version of this article.)

4. Results

4.1. Generation of training samples from Sentinel-1 imagery

With the FARM framework, totals of 1240, 99, and 907 rice objects were extracted from Sentinel-1 SAR data over site A, B and C, respectively. Fig. 6 presents the distribution of rice objects (Fig. 6a-c) and detailed information on all spatial objects generated from Sentinel-1 SAR data over each study site (Fig. 6d-k). Despite the uneven distribution of rice objects across the study area, they were still able to provide a reliable indication of the distribution of rice at each study site. The rice objects in site A were distributed along the banks of the Qixing River. The rice objects of site B are sparser than those of site A and site C because of the complex planting structure in this area. The rice objects in site C were distributed mainly in coastal plains, basins, and plains between hills.

Fig. 6d-k shows the details of the different representative subsets selected from each study area. Considering the complexity of the planting structures in different study sites, to better display the details, the subset sizes were set to 3×3 km, 1×1 km, and 1×1 km at sites A, B and C, respectively. Compared to cropland objects (dark green), the over segmentation of non-cropland objects, such as natural vegetation

(green) (Fig. 6e), built-up areas (purple) (Fig. 6f) and water bodies (dark) (Fig. 6k), was more obvious. Cropland objects and non-cropland objects could be separated effectively. Furthermore, the spatial sizes of the final rice objects were usually smaller than those of other crop objects; this is consistent with the existing research (Ozdarici Ok and Akyurek, 2012; Zhang et al., 2021). Finally, non-rice samples and rice samples were randomly arranged and generated in a 1:1 ratio.

4.2. Classification map of paddy rice and accuracy assessment

4.2.1. Performance of FARM for sites A-C in China

The paddy rice distribution maps at a 10-m spatial resolution across study sites A, B and C were generated using our proposed method (Fig. 7). The maps presented in Fig. 7(a-c) offer a comprehensive view of the size and scope of paddy rice fields across three study sites. Generally, the final rice distribution at each study site was consistent with the rice object distribution in Fig. 6, and rice was distributed mostly in flat areas with low elevations. Fig. 7(d-k) display zoomed-in views of detailed areas outlined by red rectangles in Fig. 7(a-c). The FARM framework proposed in this study can efficiently distinguish rice fields from other types of land cover, and there is a clear separation between each crop land parcel and road (Fig. 7d, f, h, i, j).

Table 3

Accuracy assessment of the classification map produced by the FARM framework at the study sites A-C in 2021.

Study area	Reference	Classification map		PA (%)	UA (%)	OA (%)	F1-score (%)
		Rice	Non-rice				
Site A	Rice	274	9	96.82	99.28	97.94	98.03
	Non-rice	2	249				
Site B	Rice	196	45	81.33	99.49	90.73	89.50
	Non-rice	1	254				
Site C	Rice	250	25	90.91	97.28	93.13	93.99
	Non-rice	7	184				

For site A in Heilongjiang Province with large-scale agricultural estates and intensified rice cultivation, paddy rice is a major crop in most parts of the region except for the central area (Fig. 7a). Fig. 7(g) depicts the good discrimination of FARM framework between paddy rice and natural wetland. Site B in Zhejiang Province has small fields and scattered rice-planting areas, and the eastern regions are the primary distribution areas for rice (Fig. 7b). For site C, only the late rice planting areas were identified. Similar to site B, the major rice cultivation regions in study site C are scattered and are mainly distributed in low-altitude regions, including the northern and southern regions (Fig. 7c). Furthermore, salt-and-pepper noise was very slight in this method with

reliable samples and a multi-RF classification strategy (Fig. 7h, i, j, k).

Also, the accuracies of the method at the three study sites were quantitatively assessed using 534, 496, and 466 samples for study sites A, B and C, respectively. The OA and F1-score values of the classification maps obtained with FARM were 97.94%, 98.03% at study site A, 90.73%, 89.50% at study site B, and 91.14%, 91.55% at study site C, respectively (Table 3).

4.2.2. Application of FARM for site D-E in USA and Thailand

To assess the method's suitability in other rice-growing countries, we chose California, USA, and Nakhon, Thailand, as our study sites and conducted a comprehensive validation. The results, as depicted in Fig. 8, unequivocally demonstrate the exceptional performance of the FARM method in both site D and site E, accurately depicting the spatial distribution of rice cultivation. In site D, rice cultivation areas are mainly concentrated in the southwest region, characterized by well-organized and larger rice paddies. Fig. 8(c-d) depict the spatial distribution details of paddy rice in site D along with false-color images. It is evident that the FARM method can accurately identify the spatial distribution of rice, with only a few mixed pixels between fallow land and rice fields. In site E, rice cultivation areas are more dispersed, comprising smaller and fragmented rice fields. The FARM method successfully captured the spatial planting patterns of rice. However, as shown in Fig. 8(e-f), there are still some instances of omission errors where rice and other crops are

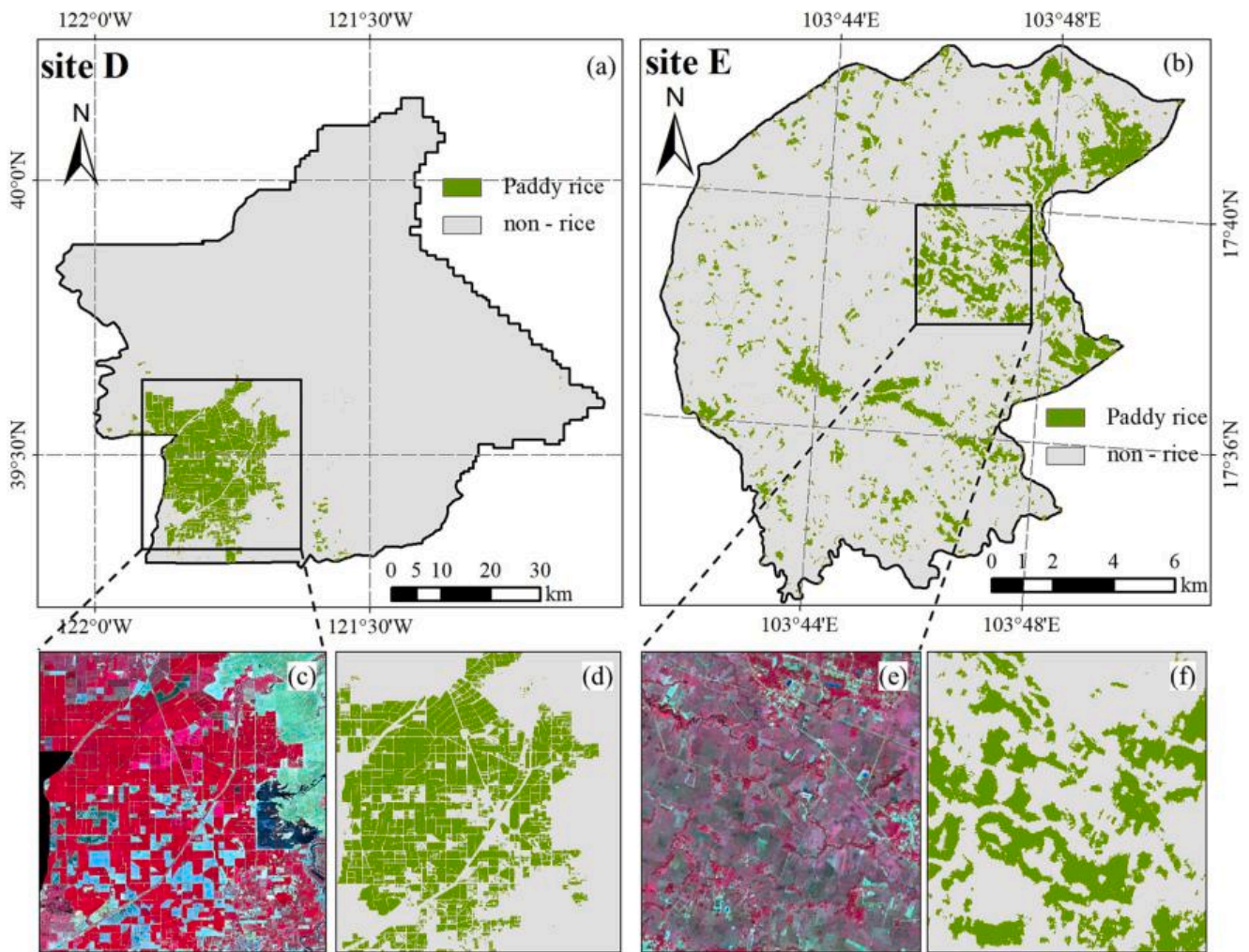


Fig. 8. Paddy rice distribution map produced by the proposed method at study site D-E (a, b) and close-up views of subsets with paddy rice objects (c, e) and related false-color composite Sentinel-2 images (R: NIR, G: Red, and B: Green) at two study sites (d, f). (For interpretation of the references to color in this figure legend, the reader is referred to the web version of this article.)

Table 4

Accuracy assessment of the classification map produced by the FARM framework at the five study sites D and E in 2021.

Study area	Reference	Classification map		PA (%)	UA (%)	OA (%)	F1-score (%)
		Rice	Non-rice				
Site D	Rice	267	26	92.13	98.16	94.83	94.51
	Non-rice	5	302				
Site E	Rice	286	59	82.90	98.96	89.67	90.22
	Non-rice	3	252				

not accurately distinguished.

Additionally, we conducted a quantitative assessment of the method's accuracy at the two study sites, using 600 samples for each site. The classification maps generated by the FARM method resulted in OA and F1-score values of 94.83% and 94.51% at study site D, and 89.67% and 90.22% at study site E, respectively (Table 4).

4.3. Comparison of FARM with other methods

Fig. 9 presents the accuracy comparison among FARM and the four other previously proposed methods (VH_{pixels}-SARFS, VH_{objects}-SPRI, SAR_{objects}-RF, and Optical_{pixels}-RF) listed in Subsection 3.4 for site A-C. Among the index-based methods, VH_{pixels}-SARFS performed better at site A, but at sites B and C, which have complex land structures, the pixel-based SARFS method could not effectively distinguish rice from other land cover types. The OA was poor, reaching only 44.65% at site C. Correspondingly, VH_{objects}-SPRI exhibited high PAs at all three study sites, indicating that the omission error of rice in this method was small, but at site A, the method had a large commission error, and the UA was only 57.38%. The supervised SAR_{objects}-RF, Optical_{pixels}-RF and FARM, which were trained using the samples obtained in this paper, generally achieved better performances than the index-based methods. Nonetheless, the SAR_{objects}-RF method still had a large commission error at site A, and the performances of Optical_{pixels}-RF at site B and site C with complex crop-planting structures were still worse than the FARM performances.

Furthermore, Fig. 10 exhibits the evaluation of classification details obtained through five rice mapping methods across diverse land cover types. For site A, crops dominate the study area's land cover type. The five methods can effectively identify paddy rice in this study area, and the omission error of rice is small. However, the VH_{objects}-SPRI method and the SAR_{objects}-RF method perform poorly when distinguishing between rice and other crops (Fig. 10 i, j); VH_{pixels}-SARFS can accurately identify rice and other crops, but there is more speckle noise (Fig. 10 h). The performances of the Optical_{pixels}-RF and FARM methods are basically the same, including in regions where rice cultivation is intercropped with other crops (Fig. 10 k, l), but the Optical_{pixels}-RF method is poor in distinguishing between wetlands and rice (Fig. 10 w). For site B and site C with complex planting structures and fragmented plots, VH_{pixels}-SARFS cannot accurately identify the spatial pattern of rice and is limited by the resolution of the SAR data itself and the influence of

speckle noise (Fig. 10 z, al, ax). The classification performance of the VH_{objects}-SPRI method is remarkably superior of the VH_{pixels}-SARFS method. However, this method still a serious mixture problem among rivers, other crops, paddy fields and rice (Fig. 10 ag, as, bf). The same commission errors also appeared in the SAR_{objects}-RF method and Optical_{pixels}-RF method (Fig. 10 ah, ai, at, au, bg, bh). The commission error of the Optical_{pixels}-RF method was concentrated mainly along the embankments of rivers and along the ridges of paddy fields (Fig. 10 au, bh).

4.4. Transferability of FARM across years

When applying the training samples from 2021 to different years, the paddy rice maps generally exhibit similar spatial patterns (Fig. 11 a-c) as the map in Fig. 7 (a-c). Fig. 11 shows the details of the classification results of the migration samples in 2020/2022. It can be seen that, apart from some misclassification errors concentrated in the region with cloud contamination at the heading growing stage (the red ellipse in Fig. 11 d), the migration samples can still identify the rice in a new year (Fig. 11 e, f, g). Specifically, Fig. 11-f shows that the transferred samples from the FARM framework can accurately capture the newly added rice planting area, and at the same time, Fig. 11-g indicates that the method is equally accurate for the conversion of rice-growing areas to non-rice areas (the yellow ellipse in Fig. 11 f, g). Additionally, when validated with the validation data, the OAs of each study site were still above 80%, 97.57%, 84.28% and 89.27% at site A (2020), site B (2022) and site C (2022), respectively (Table 5).

To further explore the method's applicability for early-season rice identification in a new year, we compared the classification results obtained based on the samples updated at the heading growing stage in the new year (2020 for site A and 2022 for sites B and C) with the results obtained using the complete FARM framework. The assessment results of accuracy are presented in Table 5. It is evident that the accuracy of the classification method using the migration samples in 2020/2022 is basically close to the classification results obtained by using the FARM framework throughout the whole year in 2020/2022.

5. Discussion

5.1. The effect of training samples on paddy rice mapping

Exploring how the size and purity of training samples impact the multi-RF classification performance within the FARM framework is necessary because the quantity and quality of training samples, as well as the equalization of samples, have important influences on the classifier's accuracy. Specifically, the quantity of samples affects the efficiency of the classifier, while the balance of different types of samples influences the classification accuracy. To address this issue, we examined the performances of varied quantities of rice and non-rice training samples automatically obtained in Section 3.2, ranging from 350 to 3,500 pixels, with a step size of 350 pixels for each study site (Fig. 12).

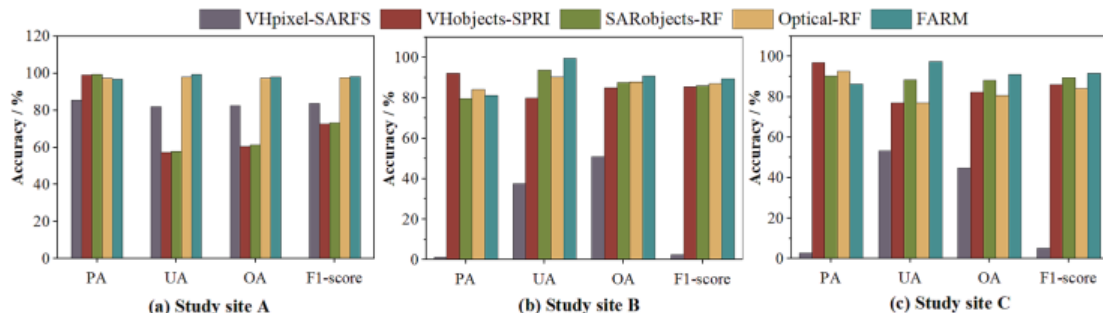


Fig. 9. Accuracy comparison of paddy rice maps obtained with five methods at study sites A-C.

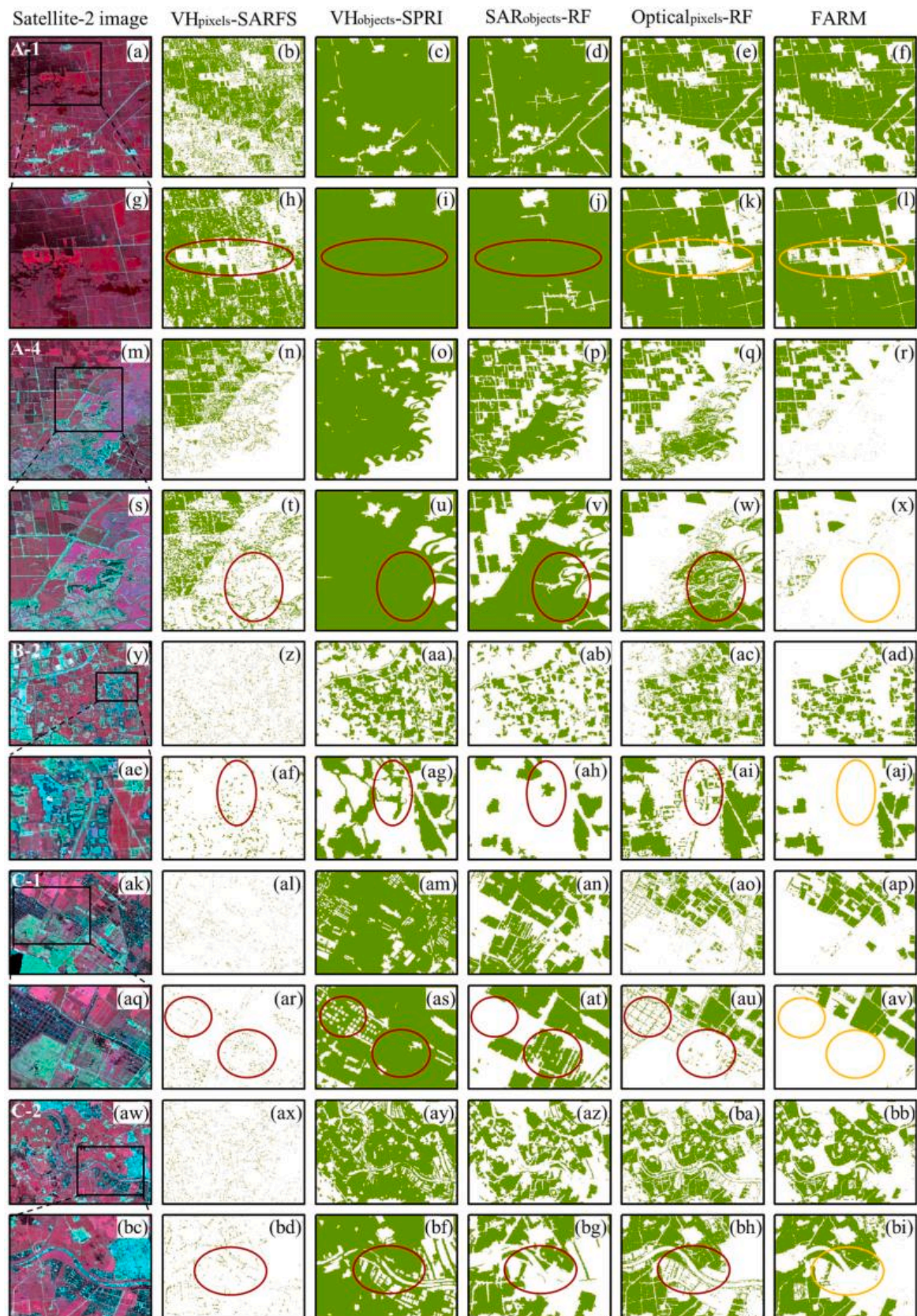


Fig. 10. Details of the rice map obtained for each study site in China with different methods. (a), (g), (m), (s), (y), (ae), (ak), (aq), (aw) and (bc) show close-up views of subsets with false-color composited Satellite-2 images during the growing peak period (R: NIR, G: Red, and B: Green). The red ellipse box indicates the error classification details, and the yellow ellipse box indicates the correct classification details. (For interpretation of the references to color in this figure legend, the reader is referred to the web version of this article.)

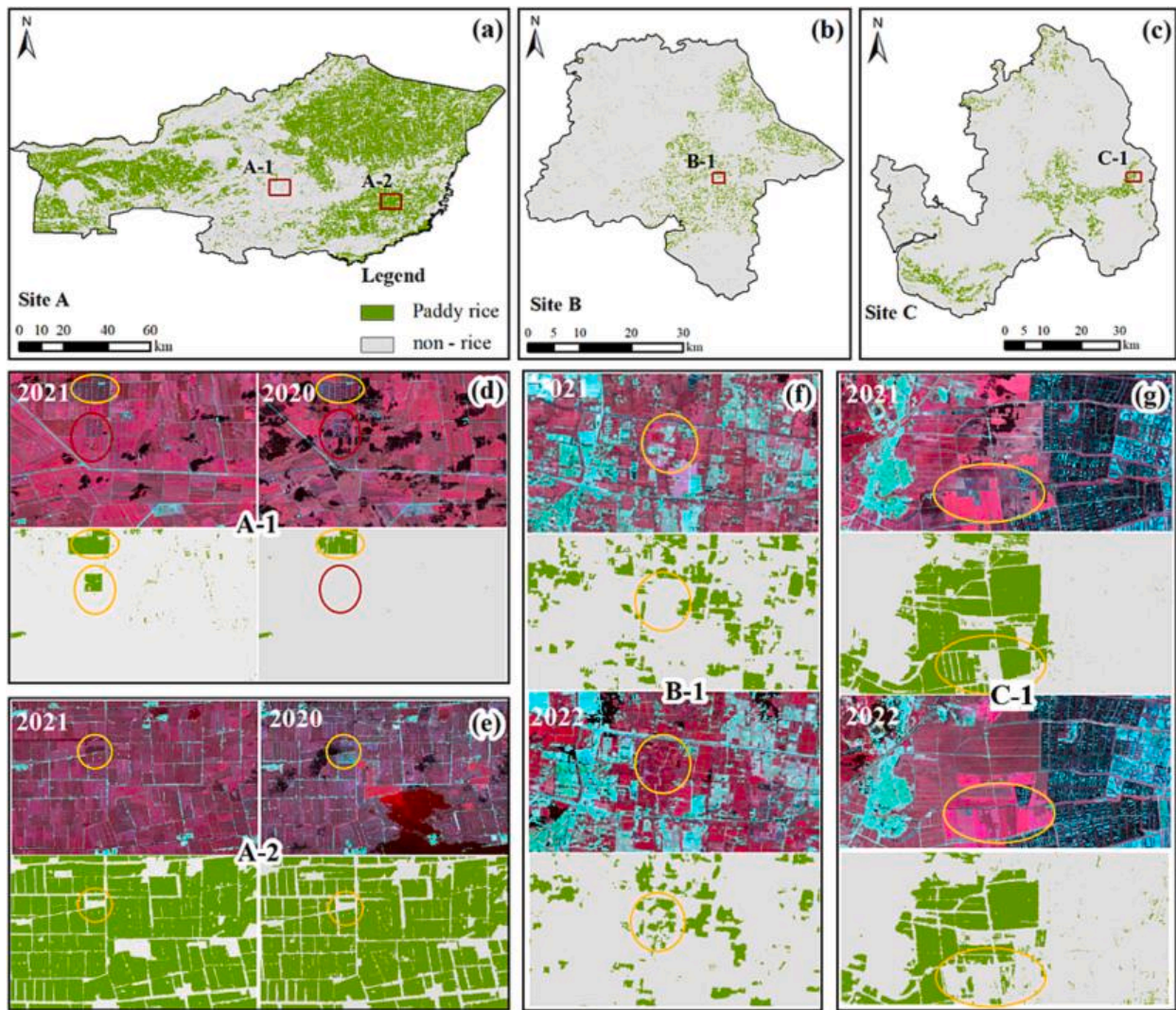


Fig. 11. The paddy rice distribution maps of 2022 obtained using the FARM framework trained with samples from 2021 (a-c) and the close-up views of four subsets of three study sites A-C with false-color composited Satellite-2 images during the peak growing period (R: NIR, G: Red, and B: Green) (d-g). The red ellipse box indicates the error classification details, and the yellow ellipse box indicates the correct classification details. (For interpretation of the references to color in this figure legend, the reader is referred to the web version of this article.)

Table 5

Accuracy assessment results of the classification maps produced by the FARM framework at three study sites A-C across years.

	Location	PA (%)	UA (%)	OA (%)	F1-score (%)
Samples from 2020/2022	Site A (2020)	98.23	99.29	98.69	98.76
	Site B (2022)	68.88	97.65	84.07	80.78
	Site C (2022)	89.09	96.84	91.85	92.80
Samples from 2021	Site A (2020)	98.23	97.20	97.57	97.72
	Site B (2022)	70.04	92.02	84.28	79.54
	Site C (2022)	88.36	93.10	89.27	90.67

The illustration in Fig. 12 shows that when the quantity of rice/non-rice samples was fixed, the performance of FARM improved as the size of non-rice/rice samples increased. At site A, due to the simple planting structure, all validation metrics remained relatively stable as the

number of rice samples gradually increased, with the quantity of non-rice samples fixed (Fig. 12 a). However, the imbalanced class distribution within the training data was a significant factor contributing to the classifier's inability to accurately identify rice, especially in areas with complex cropping conditions. Based on this analysis, it is recommended to balance the quantity of rice and non-rice samples to stabilize the performances of supervised classifiers when using the FARM framework for rice mapping. Additionally, Fig. 12 (c), (f), and (i) demonstrate that when the sample sizes of the rice and non-rice samples were changed simultaneously, the difference in the precision change of the FARM was small, indicating that the FARM framework remains applicable even when working with a limited sample size.

Furthermore, we examined the impact of training sample purity on the accuracy of the FARM framework by adding random noise to 3500 pixels of pure rice and non-rice training samples. Specifically, we evaluated the accuracy of the FARM framework by introducing noise pixels at intervals of 10% to 50%, with steps of 10%. Fig. 13 indicates that the performance of FARM decreases as the level of noise in the rice and non-rice samples increases. For site A, all the validation metrics remained relatively unchanged even when the non-rice training samples contain 50% noise, suggesting that the method may benefit from the simple planting mode of site A (Fig. 13 b). However, in contrast, as the ratio of

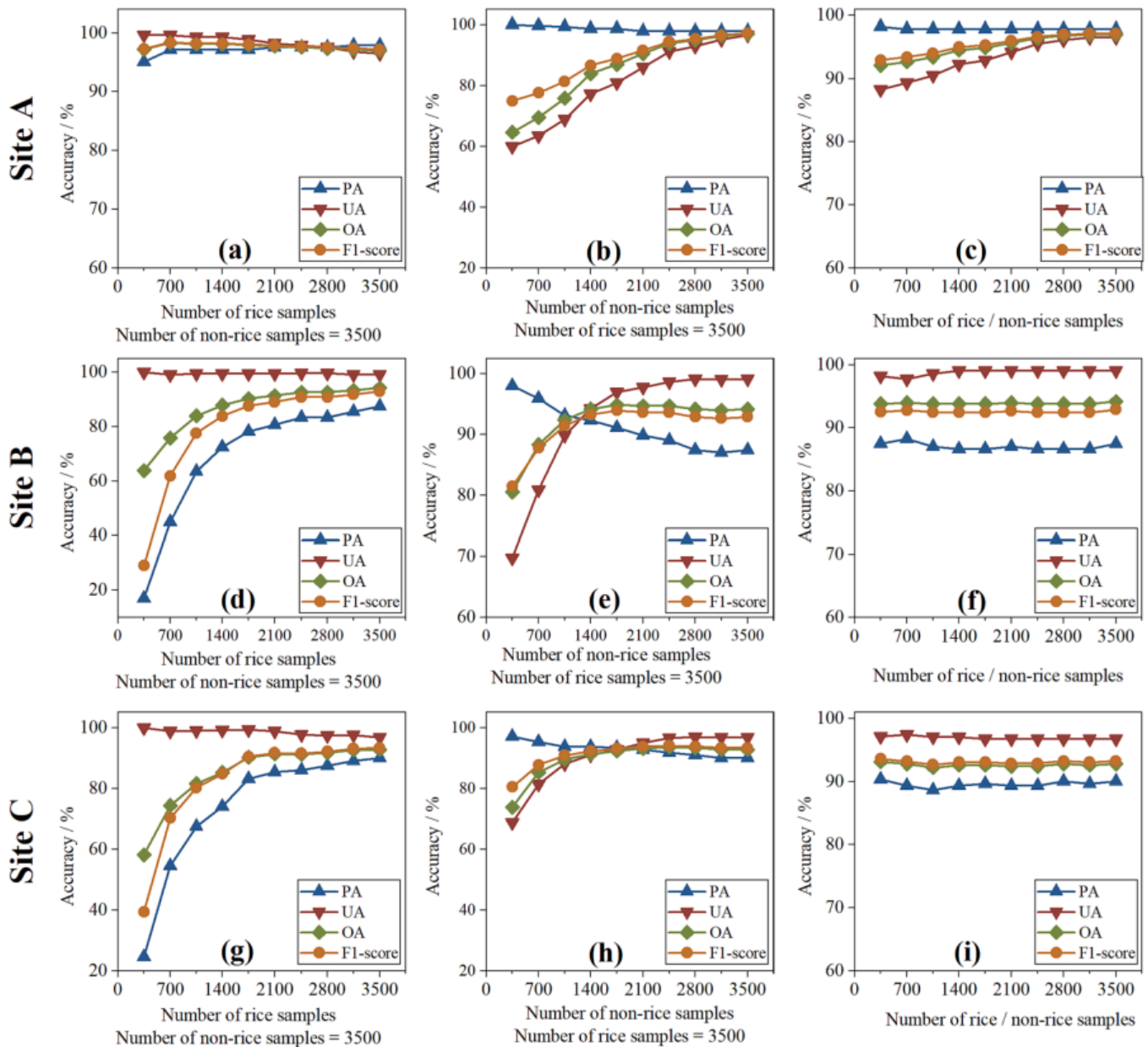


Fig. 12. The changes in each validation metric of the FARM framework under varied quantities of training samples at each study site. (a), (d), and (g) illustrate the changes in all the validation metrics when the quantity of rice samples is changed and the quantity of non-rice samples is fixed at 3,500 at each study site; (b), (e), and (h) illustrate the changes in all the validation metrics when the quantity of non-rice samples is fixed at 3,500 and the quantity of rice samples is fixed at 3,500 at each study site; and (c), (f), and (i) illustrate the changes in all the validation metrics when the quantity of rice samples and non-rice samples are changed by the same magnitude at each study site.

noise increased to 50% for both rice and non-rice training samples, the accuracy of the FARM framework drastically declined, making it almost ineffective in distinguishing between images of rice and non-rice. Nevertheless, the accuracy of the FARM framework remained robust and generally maintained a high level of performance ($>80\%$) at each study site where the noise proportion was kept under 30%, with only a slight reduction in accuracy observed. The FARM method exhibits strong resilience to the quality of rice/non-rice training samples obtained through SAR data.

5.2. The applicability of the FARM framework in early-season rice identification

The classification performance was tested when the time-series images were gradually increased at all three study sites in China to analyze

the impact of the applicability of the FARM framework in early-season rice identification, as shown in Fig. 14. When the time-series images were gradually increased, each validation metric gradually increased, and the rice identification accuracy underwent a small rapid increase during the rice transplanting period. Additionally, when the rice was at the heading stage, the mapping accuracy of the FARM framework reached a stable state, suggesting that the transplanting stage and heading stage are the best phenological periods for identifying paddy rice. Furthermore, the practicability of using the fully automatic samples acquired by the FARM framework in interannual migration is illustrated in Section 4.4. As a result, by using the training samples obtained by sample migration in historical years, we completed an annual update of the rice planting distribution around the rice heading date.

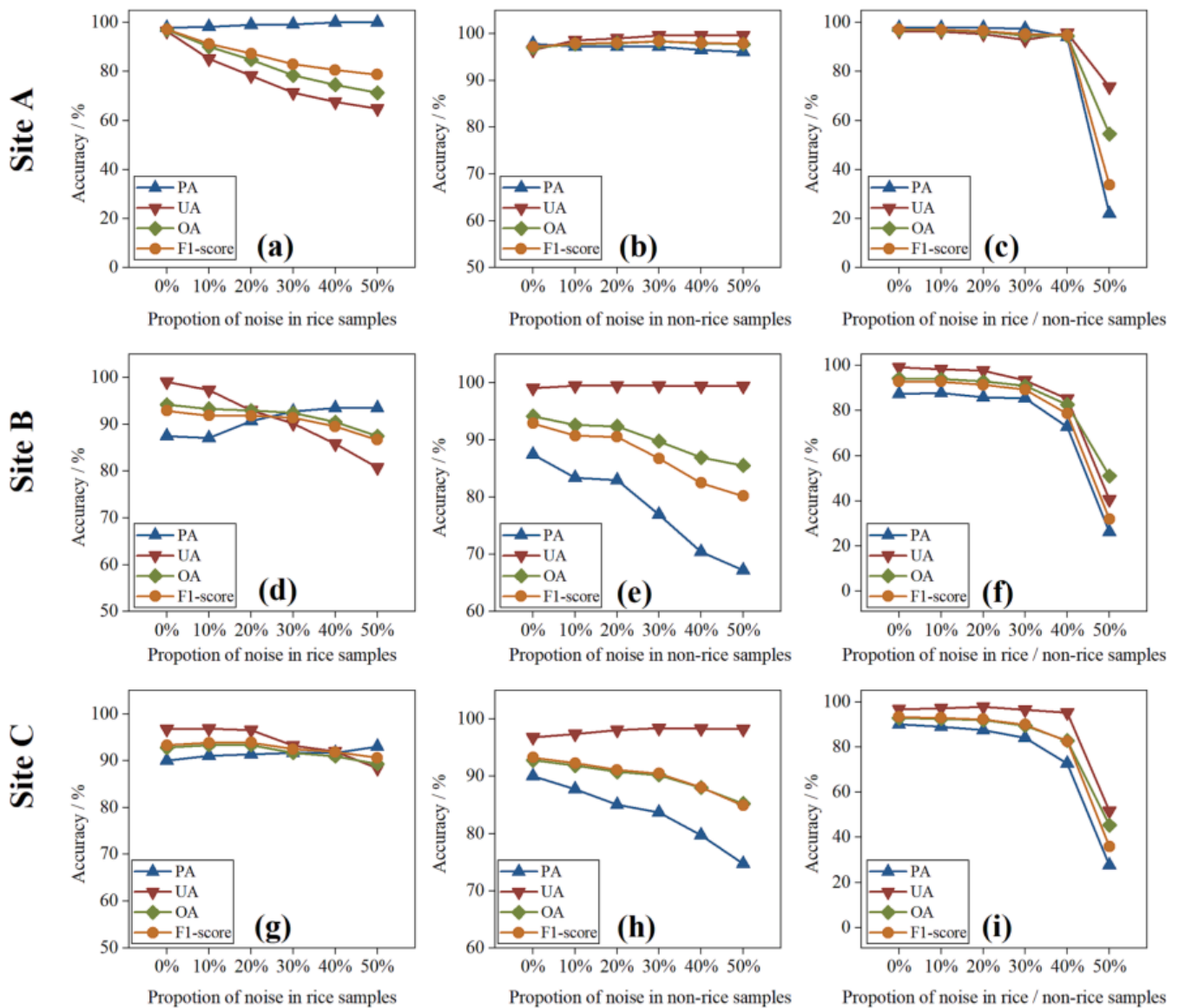


Fig. 13. The changes in each validation metric of the FARM framework under different proportions of noise in the automated training sample generation method at each study site. (a), (d), and (g) illustrate the changes in all the validation metrics when the proportion of rice samples at each study site is changed; (b), (e), and (h) illustrate the changes in all the validation metrics when the proportion of non-rice samples at each study site is changed; and (c), (f), and (i) illustrate the changes in all the validation metrics when the proportion of rice samples and non-rice samples are changed with the same magnitude at each study site.

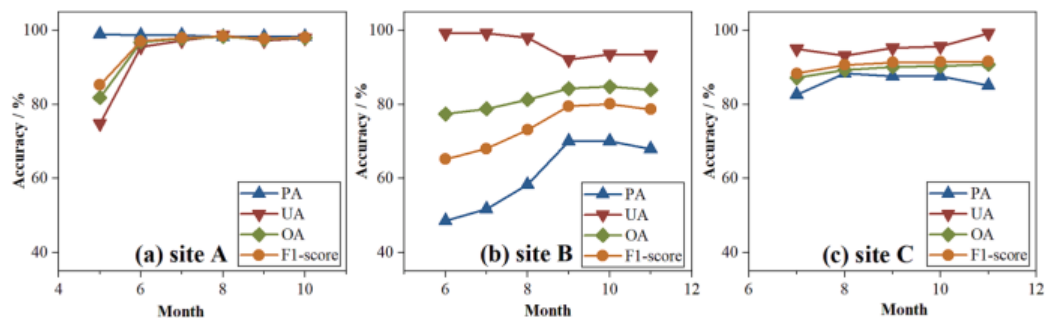


Fig. 14. The changes in each validation metric of the FARM framework with paddy rice progress. (a) shows the changes in each validation metric for site A in 2020; (b) shows the changes in each validation metric for site B in 2022; and (c) shows the changes in each validation metric for site C in 2022.

5.3. Limitations and prospects

To determine the appropriate flooding periods of rice using the

FARM framework, it is necessary to have data on rice phenology. In this study, the dates for rice phenology were obtained from some publicly accessible international data websites (Table 1). However, the lack of

available crop calendar data in some regions of the world may limit the application of FARM framework in large-scale rice mapping. Regarding this issue, several researchers have produced various global rice phenology date products (Boschetti et al., 2017; Laborte et al., 2017; Luo et al., 2020). Additionally, Zhao et al. (2023) conducted studies on an automated simulation method of crop phenology using optical satellite images. These products or methods have the potential to improve the accuracy of FARM and open up avenues for a more comprehensive automatic crop identification approach in the future.

In our study, the object-based strategy was adopted only when obtaining automatic training samples. Through the SNIC method, the segmentation of each ground object and the extraction of rice and non-rice training samples were completed based on the annual key radar features. However, considering the over-segmentation of non-cropland objects and parts of rice objects, the pixel-based strategy was still used to complete the final classification of optical images using multi-RF. However, salt and pepper noise inevitably exists in pixel-based classification methods, and this affects the final classification accuracy (Xu et al., 2023). As a result, cloud-free optical images can be used as auxiliary data for segmentation, and the whole rice-mapping framework can be completed on the object scale.

6. Conclusions

In this study, we proposed a fully automated rice mapping (FARM) framework by combining time-series SAR imagery with optical satellite imagery to enable large-scale rice mapping without the need to manually collect any samples. Firstly, to address the issue that machine learning requires a large number of labeled samples, we proposed an object-based automatic labeling method for training samples based on radar phenological characteristics. Additionally, to utilize the optical image information to the greatest extent and considering the impact of clouds on optical images, we constructed a multi-RF classification strategy to fuse different optical and SAR image classification results in the decision-making stage and complete the final fully automatic rice recognition.

We evaluated the robustness of the FARM framework and explored its ability when training samples were transferred to other years. The proposed method was tested based on three study sites in China, one site in the USA and one site in Thailand. The experimental results show that the FARM outperformed other baseline methods in terms of its accuracy and stability at all five study sites. Future work will involve adopting the FARM framework for national-scale rice mapping and extending the method to early-season rice identification. The latest release of FARM can be viewed at <https://feature-selected.users.earthengine.app/view/farm> and the code is available on GitHub with the link <https://github.com/gactyxc/FARM.git>.

CRedit authorship contribution statement

Yuan Gao: Methodology, Software, Validation, Writing – original draft, Writing – original draft, Writing – review & editing. **Yaozhong Pan:** Methodology, Writing – review & editing. **Xiufang Zhu:** Writing – original draft. **Le Li:** Writing – original draft. **Shoujia Ren:** Validation. **Chuanwu Zhao:** Validation. **Xuechang Zheng:** Validation.

Declaration of Competing Interest

The authors declare that they have no known competing financial interests or personal relationships that could have appeared to influence the work reported in this paper.

Data availability

Data will be made available on request.

Acknowledgements

This research was funded by the National Natural Science Foundation of China Major Program (Grant No. 42192581), the National High-Resolution Earth Observation System (The Civil Part) Technology Projects of China (No. 20-Y30F10-9001-20/22), and the Open Fund of State Key Laboratory of Remote Sensing Science and Beijing Engineering Research Center for Global Land Remote Sensing Products (Grant No. OF202209).

References

- Achanta, R., Süsstrunk, S., 2017. Superpixels and polygons using simple non-iterative clustering. In: 2017 IEEE Conference on Computer Vision and Pattern Recognition (CVPR). Presented at the 2017 IEEE Conference on Computer Vision and Pattern Recognition (CVPR), pp. 4895–4904. <https://doi.org/10.1109/CVPR.2017.520>.
- Belgiu, M., Csillik, O., 2018. Sentinel-2 cropland mapping using pixel-based and object-based time-weighted dynamic time warping analysis. *Remote Sens. Environ.* 204, 509–523. <https://doi.org/10.1016/j.rse.2017.10.005>.
- Boschetti, M., Busetto, L., Manfron, G., Laborte, A., Asilo, S., Pazhanivelan, S., Nelson, A., 2017. PhenoRice: a method for automatic extraction of spatio-temporal information on rice crops using satellite data time series. *Remote Sens. Environ.* 194, 347–365. <https://doi.org/10.1016/j.rse.2017.03.029>.
- Bouvet, A., Le Toan, T., 2011. Use of ENVISAT/ASAR wide-swath data for timely rice fields mapping in the Mekong River Delta. *Remote Sens. Environ.* 115, 1090–1101. <https://doi.org/10.1016/j.rse.2010.12.014>.
- Chandrasekar, K., Sessa Sai, M.V.R., Roy, P.S., Dwevedi, R.S., 2010. Land surface water index (LSWI) response to rainfall and NDVI USING the MODIS vegetation index product. *Int. J. Remote Sens.* 31, 3987–4005. <https://doi.org/10.1080/01431160802575653>.
- Chen, J., Huang, J., Hu, J., 2011. Mapping rice planting areas in southern China using the China Environment Satellite data. *Math. Comput. Model.*, Mathematical and Computer Modeling in agriculture (CCTA 2010) 54, 1037–1043. [10.1016/j.mcm.2010.11.033](https://doi.org/10.1016/j.mcm.2010.11.033).
- Clauss, K., Ottinger, M., Kuenzer, C., 2018. Mapping rice areas with Sentinel-1 time series and superpixel segmentation. *Int. J. Remote Sens.* 39, 1399–1420. <https://doi.org/10.1080/01431161.2017.1404162>.
- Dong, J., Xiao, X., 2016. Evolution of regional to global paddy rice mapping methods: a review. *ISPRS J. Photogramm. Remote Sens.* 119, 214–227. <https://doi.org/10.1016/j.isprsjprs.2016.05.010>.
- Dong, J., Xiao, X., Menarguez, M.A., Zhang, G., Qin, Y., Thau, D., Biradar, C., Moore, B., 2016. Mapping paddy rice planting area in northeastern Asia with Landsat 8 images, phenology-based algorithm and Google Earth Engine. *Remote Sens. Environ.*, Landsat 8 Science Results 185, 142–154. <https://doi.org/10.1016/j.rse.2016.02.016>.
- Hansen, M.C., Egorov, A., Potapov, P.V., Stehman, S.V., Tyukavina, A., Turubanova, S.A., Roy, D.P., Goetz, S.J., Loveland, T.R., Ju, J., Kommareddy, A., Kovalsky, V., Forsyth, C., Bents, T., 2014. Monitoring conterminous United States (CONUS) land cover change with Web-Enabled Landsat Data (WELD). *Remote Sens. Environ.* 140, 466–484. <https://doi.org/10.1016/j.rse.2013.08.014>.
- Hao, P., Di, L., Zhang, C., Guo, L., 2020. Transfer Learning for Crop classification with Cropland Data Layer data (CDL) as training samples. *Sci. Total Environ.* 733, 138869. <https://doi.org/10.1016/j.scitotenv.2020.138869>.
- Hripcsak, G., Rothschild, A.S., 2005. Agreement, the F-measure, and reliability in information retrieval. *J. Am. Med. Inform. Assoc.* 12, 296–298. <https://doi.org/10.1197/jamia.M1733>.
- Jin, C., Xiao, X., Dong, J., Qin, Y., Wang, Z., 2016. Mapping paddy rice distribution using multi-temporal Landsat imagery in the Sanjiang Plain, northeast China. *Front. Earth Sci.* 10, 49–62. <https://doi.org/10.1007/s11707-015-0518-3>.
- Keppler, F., Hamilton, J.T.G., Braß, M., Röckmann, T., 2006. Methane emissions from terrestrial plants under aerobic conditions. *Nature* 439, 187–191. <https://doi.org/10.1038/nature04420>.
- Kuenzer, C., Knauer, K., 2013. Remote sensing of rice crop areas. *Int. J. Remote Sens.* 34, 2101–2139. <https://doi.org/10.1080/01431161.2012.738946>.
- Laborte, A.G., Gutierrez, M.A., Balanza, J.G., Saito, K., Zwart, S.J., Boschetti, M., Murty, M.V.R., Villano, L., Aunario, J.K., Reinke, R., Koo, J., Hijmans, R.J., Nelson, A., 2017. RiceAtlas, a spatial database of global rice calendars and production. *Sci. Data* 4, 170074. <https://doi.org/10.1038/sdata.2017.74>.
- Linquist, B.A., Adviento-Borbe, M.A., Pittelkow, C.M., van Kessel, C., van Groenigen, K. J., 2012. Fertilizer management practices and greenhouse gas emissions from rice systems: a quantitative review and analysis. *Field Crops Res.* 135, 10–21. <https://doi.org/10.1016/j.fcr.2012.06.007>.
- Luo, C., Qi, B., Liu, H., Guo, D., Lu, L., Fu, Q., Shao, Y., 2021. Using time series Sentinel-1 images for object-oriented crop classification in google earth engine. *Remote Sens.* 13, 561. <https://doi.org/10.3390/rs13040561>.
- Luo, Y., Zhang, Z., Chen, Y., Li, Z., Tao, F., 2020. ChinaCropPhen1km: a high-resolution crop phenological dataset for three staple crops in China during 2000–2015 based on leaf area index (LAI) products. *Earth Syst. Sci. Data* 12, 197–214. <https://doi.org/10.5194/essd-12-197-2020>.
- Nguyen, D.B., Clauss, K., Cao, S., Naeimi, V., Kuenzer, C., Wagner, W., 2015. Mapping rice seasonality in the mekong delta with multi-year Envisat ASAR WSM data. *Remote Sens.* 7. <https://doi.org/10.3390/rs71215808>.

- Nguyen, D.B., Gruber, A., Wagner, W., 2016. Mapping rice extent and cropping scheme in the Mekong Delta using Sentinel-1A data. *Remote Sens. Lett.* 7, 1209–1218. <https://doi.org/10.1080/2150704X.2016.1225172>.
- Ni, R., Tian, J., Li, X., Yin, D., Li, J., Gong, H., Zhang, J., Zhu, L., Wu, D., 2021. An enhanced pixel-based phenological feature for accurate paddy rice mapping with Sentinel-2 imagery in Google Earth Engine. *ISPRS J. Photogramm. Remote Sens.* 178, 282–296. <https://doi.org/10.1016/j.isprsjprs.2021.06.018>.
- Ozdarici Ok, A., Akyurek, Z., 2012. A segment-based approach to classify agricultural lands by using multi-temporal optical and microwave data. *Int. J. Remote Sens.* 33, 7184–7204. <https://doi.org/10.1080/01431161.2012.700423>.
- Pan, Y., Li, L., Zhang, J., Liang, S., Zhu, X., Sulla-Menashé, D., 2012. Winter wheat area estimation from MODIS-EVI time series data using the Crop Proportion Phenology Index. *Remote Sens. Environ.* 119, 232–242. <https://doi.org/10.1016/j.rse.2011.10.011>.
- Pan, B., Shi, Z., Xu, X., 2017. Hierarchical guidance filtering-based ensemble classification for hyperspectral images. *IEEE Trans. Geosci. Remote Sens.* 55, 4177–4189. <https://doi.org/10.1109/TGRS.2017.2689805>.
- Qin, Y., Xiao, X., Dong, J., Zhou, Y., Zhu, Z., Zhang, G., Du, G., Jin, C., Kou, W., Wang, J., Li, X., 2015. Mapping paddy rice planting area in cold temperate climate region through analysis of time series Landsat 8 (OLI), Landsat 7 (ETM+) and MODIS imagery. *ISPRS J. Photogramm. Remote Sens.* 105, 220–233. <https://doi.org/10.1016/j.isprsjprs.2015.04.008>.
- Son, N.-T., Chen, C.-F., Chen, C.-R., Duc, H.-N., Chang, L.-Y., 2014. A phenology-based classification of time-series MODIS data for rice crop monitoring in Mekong Delta, Vietnam. *Remote Sens.* 6, 135–156. <https://doi.org/10.3390/rs6010135>.
- Son, N.-T., Chen, C.-F., Chen, C.-R., Toscano, P., Cheng, Y.-S., Guo, H.-Y., Syu, C.-H., 2021. A phenological object-based approach for rice crop classification using time-series Sentinel-1 Synthetic Aperture Radar (SAR) data in Taiwan. *Int. J. Remote Sens.* 42, 2722–2739. <https://doi.org/10.1080/01431161.2020.1862440>.
- Wang, S., Azzari, G., Lobell, D.B., 2019. Crop type mapping without field-level labels: random forest transfer and unsupervised clustering techniques. *Remote Sens. Environ.* 222, 303–317. <https://doi.org/10.1016/j.rse.2018.12.026>.
- Weiss, M., Jacob, F., Duveiller, G., 2020. Remote sensing for agricultural applications: a meta-review. *Remote Sens. Environ.* 236, 111402. <https://doi.org/10.1016/j.rse.2019.111402>.
- Xiao, X., Boles, S., Frolking, S., Salas, W., Moore, B., Li, C., He, L., Zhao, R., 2002. Observation of flooding and rice transplanting of paddy rice fields at the site to landscape scales in China using VEGETATION sensor data. *Int. J. Remote Sens.* 23, 3009–3022. <https://doi.org/10.1080/01431160110107734>.
- Xiong, J., Thenkabail, P.S., Gumma, M.K., Teluguntla, P., Poehnell, J., Congalton, R.G., Yadav, K., Thau, D., 2017. Automated cropland mapping of continental Africa using Google Earth Engine cloud computing. *ISPRS J. Photogramm. Remote Sens.* 126, 225–244. <https://doi.org/10.1016/j.isprsjprs.2017.01.019>.
- Xu, S., Zhu, X., Chen, J., Zhu, X., Duan, M., Qiu, B., Wan, L., Tan, X., Xu, Y.N., Cao, R., 2023. A robust index to extract paddy fields in cloudy regions from SAR time series. *Remote Sens. Environ.* 285, 113374. <https://doi.org/10.1016/j.rse.2022.113374>.
- Xuan, F., Dong, Y., Li, J., Li, X., Su, W., Huang, X., Huang, J., Xie, Z., Li, Z., Liu, H., Tao, W., Wen, Y., Zhang, Y., 2023. Mapping crop type in Northeast China during 2013–2021 using automatic sampling and tile-based image classification. *Int. J. Appl. Earth Obs. Geoinformation* 117, 103178. <https://doi.org/10.1016/j.jag.2022.103178>.
- Yang, G., Yu, W., Yao, X., Zheng, H., Cao, Q., Zhu, Y., Cao, W., Cheng, T., 2021. AGTOC: a novel approach to winter wheat mapping by automatic generation of training samples and one-class classification on Google Earth Engine. *Int. J. Appl. Earth Obs. Geoinformation* 102, 102446. <https://doi.org/10.1016/j.jag.2021.102446>.
- Zhan, P., Zhu, W., Li, N., 2021. An automated rice mapping method based on flooding signals in synthetic aperture radar time series. *Remote Sens. Environ.* 252, 112112. <https://doi.org/10.1016/j.rse.2020.112112>.
- Zhang, H., Liu, W., Zhang, L., 2022. Seamless and automated rapeseed mapping for large cloudy regions using time-series optical satellite imagery. *ISPRS J. Photogramm. Remote Sens.* 184, 45–62. <https://doi.org/10.1016/j.isprsjprs.2021.12.001>.
- Zhang, C., Zhang, H., Zhang, L., 2021. Spatial domain bridge transfer: an automated paddy rice mapping method with no training data required and decreased image inputs for the large cloudy area. *Comput. Electron. Agric.* 181, 105978. <https://doi.org/10.1016/j.compag.2020.105978>.
- Zhao, X., Nishina, K., Akitsu, T.K., Jiang, L., Masutomi, Y., Nasahara, K.N., 2023. Feature-based algorithm for large-scale rice phenology detection based on satellite images. *Agric. For. Meteorol.* 329, 109283. <https://doi.org/10.1016/j.agrformet.2022.109283>.